Efficient Generation of a Near-visible Frequency Comb via Cherenkov-like Radiation from a Kerr Microcomb

Xiang Guo,[1] Chang-Ling Zou,[1,2] Hojoong Jung,[1] Zheng Gong,[1] Alexander Bruch,[1] Liang Jiang,[2] and Hong X. Tang[1,*]

[1]*Department of Electrical Engineering, Yale University, New Haven, Connecticut 06511, USA*
[2]*Department of Applied Physics, Yale University, New Haven, Connecticut 06511, USA*

Optical frequency combs enable state-of-the-art applications including frequency metrology, optical clocks, astronomical measurements, and sensing. Recent demonstrations of microresonator-based Kerr frequency combs or microcombs pave the way to scalable and stable comb sources on a photonic chip. Generating microcombs in the short-wavelength range, however, has been limited by large material dispersion and optical loss. Here we demonstrate a scheme for efficiently generating microcombs near the edge of the visible spectrum in a high-Q aluminum nitride microring resonator. The enhanced Pockels effect strongly couples infrared and near-visible modes into hybrid mode pairs, which participate in the Kerr microcomb generation process and lead to strong Cherenkov-like radiation in the near-visible band an octave apart. A surprisingly high on-chip conversion efficiency of 22% is achieved from a pulsed pump laser to the near-visible comb. As a result of pulse pumping, the generated microcombs are in the chaotic state. We further demonstrate a robust frequency tuning of the near-visible comb by more than one free spectral range and apply it to the absorption spectroscopy of a water-based dye molecule solution. Our work is a step towards high-efficiency visible microcomb generation and its utilization, and it also provides insights into the significance of the Pockels effect and its strong coupling with Kerr nonlinearity in a single microcavity device.

I. INTRODUCTION

Optical frequency combs are invaluable in diverse applications, including but not limited to precision metrology [1–3], optical communication [4], arbitrary waveform generation [5], microwave photonics [6,7], astronomical measurement [8,9], and spectroscopic sensing [10–12]. The large size and demanding costs of mode-locked laser combs stimulate the need for a stable, low-cost, and compact comb source, and the whispering-gallery microresonator has brought such a breakthrough [13,14]. Microresonators provide an excellent device configuration for comb generation on a chip, benefiting from the enhanced nonlinear optic effect by the high quality factor and small mode volume, as well as the engineerable dispersion by the geometry control. Over the past decade, we have witnessed exciting progress in the investigation of microcombs, including the octave comb span [15,16], temporal dissipative Kerr solitons [17–21], dual-comb spectroscopy [12,22], and 2f-3f self-referencing [23]. Beyond these promising applications, microcombs also provide a new test bed for intriguing nonlinear physics because of

their roots in generalized nonlinear Schrodinger equations, and they allow for the fundamental studies of solitons, breathers, chaos, and rogue waves [24–28].

Despite the demanding need for visible combs for applications such as biomedical imaging [29], frequency locking [30], and astronomical calibration [8,9], demonstrating a microcomb in visible wavelengths is challenging. The large material dispersion together with elevated optical loss in most materials appear to be the main obstacles for generating and broadening the visible microcomb. Great efforts have been devoted by the research community to addressing these challenges. Only relatively narrow Kerr combs have been generated at wavelengths below 800 nm in polished calcium fluoride [31] and silica bubble [32] resonators, where quality factors are difficult to achieve for typical integrated microresonators.

In this article, we demonstrate a scheme for high-efficiency near-visible microcomb generation on a chip by combining two coherent nonlinear optical processes (the Pockels and Kerr effects) in the microresonator. We realize a modified four-wave mixing process where the pump resides in the low-loss infrared band but emits photons into the edge of the visible band directly through the strongly coupled visible-infrared mode pairs. First, the
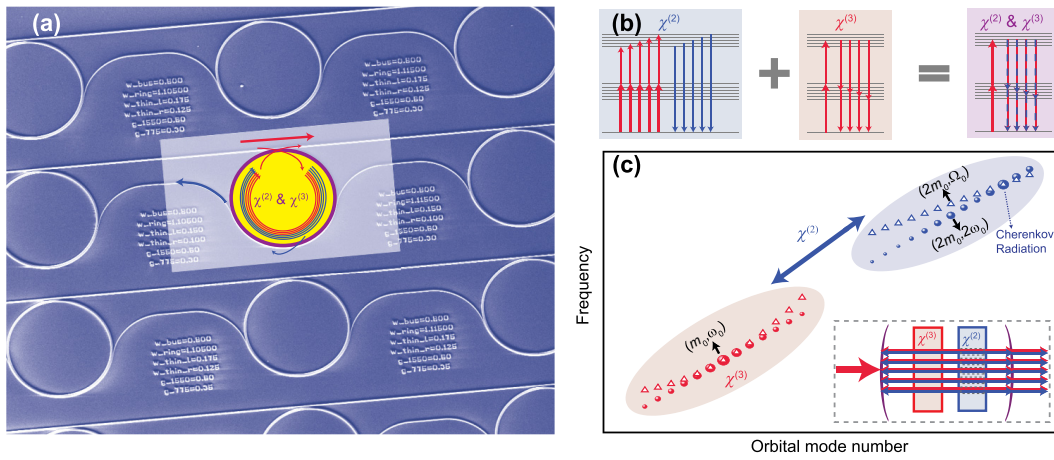
FIG. 1.   AlN microring resonator for efficient comb generation and emission in near-visible wavelengths. (a) Dual-wavelength-band frequency comb generation in a microring resonator. A single color pump is sent into a microring resonator with hybrid second- and third-order nonlinearity. After reaching the threshold of the comb generation process, the infrared part of the comb is coupled out through the top bus waveguide while the near-visible part of the comb is coupled out through the bottom wrap-around waveguide. Background: false-color SEM image of the core devices. Eight (three shown in the SEM) microrings are cascaded using one set of bus waveguides. (b) The energy diagrams of $\chi^{(2)}$, $\chi^{(3)}$ and the cascaded nonlinear interaction that involve the near-visible modes in the modified four-wave mixing process. (c) The positions of the comb lines (red and blue solid circles) and their corresponding optical modes (red and blue open triangles) in the frequency-momentum space. The size of the circles represents the intensity of the comb lines. Cherenkov-like radiation appears in the position where the near-visible comb line has the same frequency as its corresponding optical mode. Inset: schematic diagram of the dual-band comb generation process in a hybrid-nonlinearity microring cavity.

strong second-order (Pockels effect) optical nonlinearity ($\chi^{(2)}$) in aluminum nitride (AlN) microring [33] coherently couples the near-visible and infrared optical modes, which form hybrid mode pairs [34]. Mediated by these hybrid mode pairs, the near-visible modes participate in the four-wave mixing processes, which are stimulated by a pulsed pump laser at infrared wavelengths through Kerr nonlinearity ($\chi^{(3)}$). This strong hybridization of $\chi^{(2)}$-$\chi^{(3)}$ processes enables efficient comb generation in the highly dispersive near-visible wavelength band. To facilitate laser pumping and power extraction at wavelength bands separated by an octave, we load the microring with a pair of independent waveguides [35]. The infrared pump light is critically coupled to an anomalous-dispersion microring resonator through the point-contact waveguide, while the near-visible comb power is efficiently extracted by an over-coupled wrap-around waveguide. We carefully control the phase-matching condition for the $\chi^{(2)}$ process and observe a tunable Cherenkov-like radiation enhancement in the generated near-visible comb spectrum. The appearance of the Cherenkov-like radiation differentiates the current work from previous approaches of converting the infrared comb to visible wavelengths by external frequency doubling [11,36] or a weak intracavity $\chi^{(2)}$ process [37–40], behaving as the backbone for the realized high pump-to-visible comb conversion efficiency. We further show that our near-visible microcomb can be robustly tuned by more than one free spectral range through thermal tuning, a vital property for *f*-2*f* self-referencing [41]

and frequency locking to atomic transmission [30]. Lastly, we perform a proof-of-principle experiment to showcase the near-visible comb spectroscopy of a water-based dye molecule solution, which is not accessible by the more commonly available infrared comb because of the strong water absorption.

II. THEORETICAL BACKGROUND AND DEVICE DESIGN

Figure 1(a) shows a false-color scanning electron microscope (SEM) image of the fabricated microring systems. We design a series (typically eight) of microrings that share the same set of coupling waveguides but have a constant frequency offset. As a result, each microring resonator can be pumped independently, which dramatically enlarges the device parameter space that we can afford for optimal device engineering within each fabrication run. The middle inset of Fig. 1(a) shows a schematic illustration of the dual-band comb generation process in the microring. The AlN microring supports high-quality-factor (Q) optical modes ranging from near-visible (blue lines) to infrared (red lines) wavelengths. These optical modes form a variety of energy levels interconnected by second- and third-order nonlinearity, giving rise to two kinds of coherent nonlinear processes [Fig. 1(b)]. First, driven by the $\chi^{(2)}$ Pockels nonlinearity, optical modes in the near-visible and infrared bands can be strongly coupled and

form hybrid modes [34]. Here in our system the near-visible modes are higher-order transverse-magnetic (TM) modes (TM_2) while the infrared modes are fundamental TM modes (TM_0). The amount of hybridization relies on the phase-matching condition of the $\chi^{(2)}$ process, which can be engineered by tuning the width of the microring [35]. Second, due to the Kerr effect ($\chi^{(3)}$), these hybrid modes participate in the microcomb generation process [13,17,20,42] and lase when the pump laser reaches a certain threshold. Therefore, the combination of strong $\chi^{(2)}$ and $\chi^{(3)}$ nonlinearity of AlN allows the efficient generation of both infrared and near-visible combs, as shown in the inset of Fig. 1(c).

Both infrared and near-visible mode families are involved in our system. The corresponding mode frequencies are $\omega_j = \omega_0 + d_1 j + d_2 j^2/2$ and $\Omega_j = \Omega_0 + D_1 j + D_2 j^2/2$, respectively, when neglecting higher-order dispersion. Here, the central infrared and near-visible modes, a_0 and b_0, have a frequency of ω_0 and Ω_0 and an orbital mode number of m_0 and $2m_0$, respectively. $j \in \mathbb{Z}$ is the relative mode number with respect to the central modes (a_0, b_0). d_1 and D_1 are the free spectral ranges, while d_2 and D_2 describe the group velocity dispersion of the corresponding mode families. We can see from the above expressions that the optical modes of infrared and near-visible wavelengths are not of equal spacing in the frequency domain, which is illustrated by the open triangles in Fig. 1(c). On the other hand, the frequencies of infrared and near-visible comb lines are of equal spacing, which can be expressed by $\omega_{j,\mathrm{comb}} = \omega_0 + d_1 j$, $\Omega_{j,\mathrm{comb}} = 2\omega_0 + d_1 j$. The positions of the comb lines are represented by the dots in Fig. 1(c). We introduce the integrated dispersion D_{int}, which describes the angular frequency difference between the optical modes and the corresponding comb lines. It is intuitive that when the integrated dispersion for the infrared ($D_{\mathrm{int,IR}} = \omega_j - \omega_{j,\mathrm{comb}}$) or near-visible ($D_{\mathrm{int,vis}} = \Omega_j - \Omega_{j,\mathrm{comb}}$) modes approach 0, the light generated in that mode will be enhanced by the resonance. As a result, in our system we should expect enhanced comb generation in the near-visible wavelength where $D_{\mathrm{int,vis}} \approx 0$ [as noted in Fig. 1(c)], which is caused by the Cherenkov-like radiation and discussed later.

The modal expansion method [17,43–45] is used to study the dynamics of our system. To deduce the nonlinear coupled mode equations involving both Kerr and Pockels nonlinear processes, we start from the Hamiltonian of our system and then apply the Heisenberg equation on it [46]. The dynamics of modes in the resonator can be described by the Hamiltonian

$$\mathscr{H} = \sum_{j=-N_1}^{N_1} \hbar \Delta_j^a a_j^\dagger a_j + \sum_{j=-N_2}^{N_2} \hbar \Delta_j^b b_j^\dagger b_j + \mathscr{H}_{\chi^{(2)}} + \mathscr{H}_{\chi^{(3)}} + \hbar \epsilon_0 (a_0 + a_0^\dagger), \quad (1)$$

where bosonic operators a_j and b_j represent the infrared and near-visible mode families, respectively. $\mathscr{H}_{\chi^{(2)}} = \sum_{j,k,l} \hbar g_{jkl}^{(2)} (a_j a_k b_l^\dagger + a_j^\dagger a_k^\dagger b_l)$ is the three-wave mixing interaction arising from the Pockels effect of AlN with a coupling strength of $g_{jkl}^{(2)}$, and $\mathscr{H}_{\chi^{(3)}}$ includes the four-wave mixing interaction (the Kerr effect) inside one mode family or between two mode families [46]. Note that $g_{jkl}^{(2)}$ is nonzero only when $j + k = l$ due to momentum conservation. With a pump field near a_0 (with a detuning δ), the frequency detunings between the comb lines and the optical modes are $\Delta_j^a = d_2 j^2 - \delta$ and $\Delta_j^b = \Omega_0 + (D_1 - d_1)j + D_2 j^2 - 2(\omega_0 + \delta)$. We first describe how the near-visible and infrared optical modes can be coupled through the Pockels effect. Under strong external pumping, the cavity field of the pump mode (a_0) can be approximated by a classical coherent field $a_0 \approx \sqrt{N_p}$, where N_p is the intracavity pump photon number. We can therefore linearize the three-wave mixing interaction and obtain the dominant coherent conversion between two mode families,

$$\mathscr{H}_{\chi^{(2)}} \approx \sum_j \hbar G_j^{(2)} (a_j b_j^\dagger + a_j^\dagger b_j), \quad (2)$$

where $G_j^{(2)} = g_{0jj}^{(2)} \sqrt{N_p}$. Despite a large difference in the frequency, the infrared (a_j) and near-visible (b_j) mode families are coupled through a nonlinear interaction, which is essentially analogous to the linear coupling between two different spatial mode families of the same wavelength [47]. This nonlinear coupling leads to the formation of visible-infrared hybrid mode pairs, which can be described by the bosonic operators as a superposition of near-visible and infrared modes (see [46] for detailed derivations),

$$A_j = \frac{1}{\mathcal{N}_{A,j}} [(\lambda_j^- - \chi_j^a) a_j + i G_j^{(2)} b_j], \quad (3)$$

$$B_j = \frac{1}{\mathcal{N}_{B,j}} [(\lambda_j^+ - \chi_j^a) a_j + i G_j^{(2)} b_j], \quad (4)$$

where $\lambda_j^\pm = \frac{1}{2}(\chi_j^a + \chi_j^b \pm \sqrt{(\chi_j^a - \chi_j^b)^2 - 4G^2})$, $\chi_j^a = -i\Delta_j^a - \kappa_j^a$, $\chi_j^b = -i\Delta_j^b - \kappa_j^b$. κ_j^a and κ_j^b denote the loss rates of mode a_j and b_j, respectively, and $\mathcal{N}_{A,j}$ and $\mathcal{N}_{B,j}$ are the normalization factors.

Combing the $\chi^{(2)}$-induced mode coupling and the Kerr effect, an effective two-mode-family Kerr comb generation [47] is obtained. The pump at the infrared band generates emissions not only into the infrared wavelengths, but also into the near-visible wavelengths. For example, a possible photon emission at a frequency of ω in the infrared wavelength can also be accumulated in a near-visible mode at a frequency of $\omega + \omega_0 + \delta$. As discussed above, we
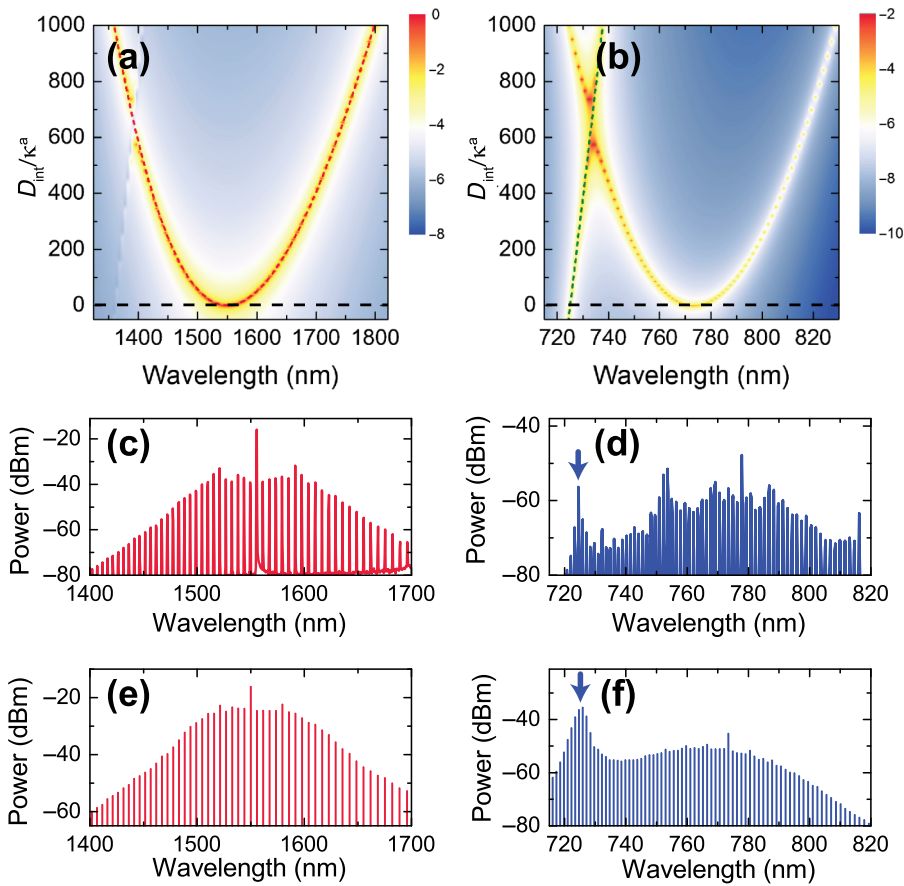
FIG. 2. Cherenkov-like radiation induced by nonlinear mode coupling. (a) The density of states for the infrared modes with a pump in the a_0 mode. Here the natural logarithm of the calculated density of states is plotted. An anomalous dispersion leads to the parabolic shape of the frequency detuning between the frequency of each comb line and that of the optical modes. The dashed red line shows the frequency detuning $D_{int(IR)}$ between the infrared comb lines and the corresponding optical modes. (b) The density of states for the near-visible modes with a pump in the a_0 mode. Here the natural logarithm of the calculated density of states is plotted. The dashed green line shows the frequency detuning $D_{int(vis)}$ between the near-visible comb lines and the corresponding optical modes. The wavelength where the near-visible comb frequency detuning $D_{int(vis)}$ approaches 0 corresponds to Cherenkov-like radiation, leading to an enhanced emission into this mode. (c),(d) The measured spectra of the infrared (c) and near-visible (d) frequency comb. The blue arrow indicates the position of Cherenkov-like radiation. (e),(f) Numerical simulations of the infrared (e) and near-visible (f) frequency comb.

expect an enhanced emission where $D_{int,vis}$ approaches 0, i.e. the near-visible comb line overlaps with its corresponding optical mode. It is convenient to quantify this on-resonance enhancement of comb generation in terms of the density of states (DOS) [46], which describes the field enhancement factor for a given optical mode and frequency detuning. Physically, the DOS is large if the frequency detuning is small and the quality factor of the mode is high. By observing the DOS at the positions where comb lines reside, we can predict the relative intensity of the generated comb lines. Figures 2(a) and 2(b) show the calculated DOS for the infrared and the near-visible modes, respectively. Here we are interested in the DOS along the $D_{int} = 0$ line (black dashed lines) in the figures, which corresponds to the positions where the comb lines appear. For the infrared band [Fig. 2(a)], the DOS along the black dashed line is symmetric around the pump. $D_{int,IR}$ is of parabolic shape as represented by the red dashed line in Fig. 2(a). However, for the near-visible wavelength [Fig. 2(b)], the DOS along the black dashed line is asymmetric, showing an enhanced DOS at 725 nm where the comb line's frequency matches the optical mode's frequency ($D_{int,vis} = 0$). Here $D_{int,vis}$ is represented by the green dashed line in Fig. 2(b). The enhanced DOS at $D_{int,vis} = 0$ greatly boosts the comb emission due to resonance

enhancement, similar to those observations induced by higher-order dispersion [20,48,49] or linear mode coupling [47,50].

III. EXPERIMENTAL MEASUREMENTS

A. Dual-wavelength-band frequency comb

The comb threshold for the current device is relatively high, around 300 mW on-chip. To easily excite the frequency comb, we pump our microring with a 100-kHz repetition rate, 10-ns-long laser system whose peak power can be several watts on-chip (see Appendix B and Supplemental Material Sec. IV for more details). As a result of pulse pumping, the current device operates in the chaotic comb generation regime. Figures 2(c) and 2(d) are the typical measurement spectra of the dual-band combs. The infrared comb spectrum is relatively symmetric around the pump wavelength, as predicted by the DOS in Fig. 2(a). For the near-visible combs, however, the spectrum is asymmetric and extends towards the short-wavelength side. The strong emission peaks near the second-harmonic wavelength (777 nm) of the pump are attributed to the large intracavity photon number near the pump wavelength, while the strong emissions centered around 725 nm [noted by the

blue arrow in Fig. 2(d)] are attributed to the Cherenkov-like radiation, which is characterized by an enhanced DOS and $D_{\mathrm{int,vis}} = 0$ as shown in Fig. 2(b). We will show later that when the large intracavity pump photon number is combined together with resonance enhancement, i.e. when the Cherenkov-like radiation wavelength is close to the second-harmonic wavelength of the pump, very efficient near-visible comb generation can be obtained. As a further confirmation of this Cherenkov-like radiation mechanism, we carry out a numerical simulation of the comb generation process using the modal expansion method [46]. Comparing the simulated results [Figs. 2(e) and 2(f)] with the experimental data, we find a valid agreement which consolidates our analysis of the physical mechanism. The residual difference between the simulation [Fig. 2(f)] and the measured results [Fig. 2(d)] can be partially attributed to a wavelength-dependent coupling efficiency between the microring and the near-visible light extraction waveguide, which increases with wavelength due to the larger evanescent field. In addition, certain other near-visible spatial mode families that are not included in our model may also get involved in the nonlinear comb generation process and lead to the discrepancy.

The optical mode number where the Cherenkov-like radiation appears (j_{CR}) should satisfy the linear phase-matching condition $D_{\mathrm{int,vis}}(j_{\mathrm{CR}}) = 0$, which corresponds to

$$j_{\mathrm{CR}} = -\frac{(D_1 - d_1)}{D_2} \pm \frac{1}{D_2}\sqrt{(D_1 - d_1)^2 - 2D_2(\Omega_0 - 2\omega_0)}.$$

(5)

According to Eq. (5), the wavelength of the Cherenkov-like radiation is related to $\Omega_0 - 2\omega_0$, which is the frequency detuning between the second harmonic of the pump and its corresponding near-visible optical mode. To verify this relation in the experiment, we change the frequency detuning $\Omega_0 - 2\omega_0$ by controlling the width of the microring, which is varied from 1.12 μm to 1.21 μm. Figures 3(a) and 3(b) show the measured dual-comb spectra generated from microrings with different widths. Note that the data in Figs. 3(a) and 3(b) are the raw data measured by the optical spectrum analyzer. We later use this data to infer the on-chip comb power by measuring the insertion loss from the chip to the optical spectrum analyzer. We find that the position of the Cherenkov-like radiation [as noted by the blue arrows in Fig. 3(b)] in the near-visible comb spectrum changes consistently from shorter to longer wavelengths with the increase of the microring width. Figure 3(c) shows the measured central wavelength of the Cherenkov-like radiation (dots) against the microring width, exhibiting a good agreement with the theoretical prediction according to Eq. (5) (solid line).

As easily observed from the comb spectra [Fig. 3(a)], the power, span, and the envelope shape of the infrared combs of different devices are quite similar because the dispersion at infrared wavelengths is not sensitive to the widths of the microring. In contrast, those of the near-visible combs change drastically [Fig. 3(b)]. In Fig. 3(d), the span of dual-band combs is summarized. We find that the appearance of Cherenkov-like radiation can help extend the span of the near-visible comb, which has been demonstrated in Kerr combs [20,49]. When the Cherenkov-like radiation appears far away from the second-harmonic wavelength of the pump [e.g. the first and last devices in Fig. 3(b)], the generated near-visible comb tends to have a broader comb span and more comb lines. On the other hand, when the wavelength of Cherenkov-like radiation is close to the second-harmonic wavelength of the pump [e.g. the fifth and sixth devices in Fig. 3(b)], there are less near-visible comb lines but the total power of the generated near-visible comb is greatly enhanced. As clearly observed in Fig. 3(e), the on-chip near-visible comb power (blue dots) varies more than 2 orders of magnitudes from 5×10^{-3} mW to 0.61 mW, while the power of the infrared comb (red dots) remains at around 0.1 mW on-chip.

An intuitive physical picture of the cascaded nonlinear process is that the comb power is first generated in the infrared modes and then partially converted to the near-visible modes through sum-frequency generation. Therefore, it is quite counterintuitive that the on-chip power of the near-visible comb can be up to ten times larger than that of the infrared comb. In fact, it is the visible-infrared hybrid mode, instead of the infrared mode only, that has become involved in the comb generation process. From this perspective, the comb power directly generates in the visible-infrared hybrid modes. Because in our device the extraction rate (from the microring to the waveguide) of the near-visible mode ($\kappa_1^b = 2\pi \times 2.6$ GHz) is much larger than that of the infrared mode ($\kappa_1^a = 2\pi \times 0.1$ GHz), the extracted comb power in the near-visible wavelength can hence be much stronger than that in the infrared wavelength. Such counterintuitive results can hardly be explained by the simple cascaded nonlinear process picture, and reaffirms the important role of the visible-infrared strong coupling in our high-efficiency near-visible comb generation process. We further investigate the dependence of comb power on the pump power, as shown in Figs. 4(c) and 4(d). When the Cherenkov-like radiation matches the second-harmonic wavelength of the pump, an increase of the comb powers with the pump is observed in both infrared and near-visible bands [Fig. 4(c)]. With a pump peak power of more than 1 W, the on-chip pump-to-comb power conversion efficiency saturates at 3% for infrared combs and 22% for near-visible combs [Fig. 4(d)]. Such high near-visible comb generation efficiency, which marks a 7 order of magnitude improvement over previous work [37], comes from a combination of the large cavity photon number near the pump wavelength, the use of an over-coupled wrap-around waveguide
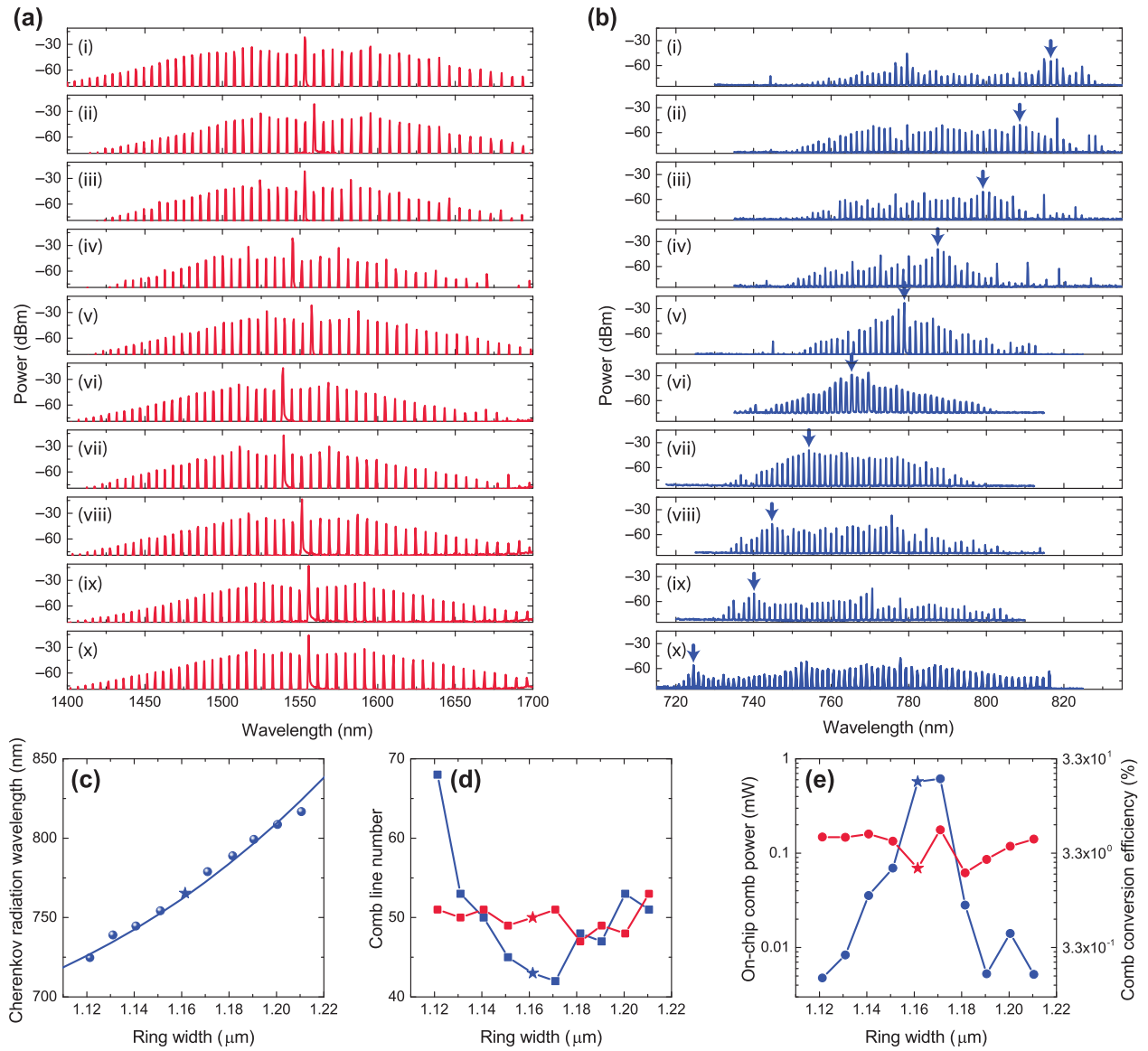
FIG. 3. Dual-wavelength-band frequency comb generated by microrings with different widths. (a) Infrared combs generated by devices with a width of 1.12 μm (bottom) to 1.21 μm (top). (b) The corresponding near-visible combs generated by devices with a width of 1.12 μm (bottom) to 1.21 μm (top). The blue arrows show the Cherenkov-like radiation wavelength. The data are measured by an optical spectrum analyzer. We later use it to infer the on-chip comb power by measuring the insertion loss from the chip to the optical spectrum analyzer. (c) Cherenkov-like radiation wavelength for devices with different microring widths. The circles correspond to the experimental data and the solid line represents the theoretical calculations. The pentagram marks the device that is used to measure the power dependence in Fig. 4. (d) The number of infrared (red) and near-visible (blue) comb lines for devices with different widths. (e) The total on-chip power of the infrared (red) and near-visible (blue) comb lines for devices with different widths.

for the near-visible comb extraction, and the Cherenkov-like radiation enhancement. As can be observed in Fig. 4(b), the DOS at $D_{\text{int,vis}} = 0$ wavelength is greatly boosted, being much larger than that observed when the Cherenkov-like radiation wavelength is far away [e.g. Fig. 2(b)]. Such large DOS finally enables the surprisingly high near-visible comb generation efficiency. The detailed comb spectra under different pump powers are shown in Supplemental Material Sec. V.

B. Thermal tuning of optical comb

The ability to continuously tune the frequency comb is vital for applications such as precision sensing, frequency locking to atomic transition, and f -$2f$ self-referencing. By tuning the temperature of the device, we obtain a continuously tunable near-visible comb by more than one free spectral range through a thermo-optic effect [51], which allows for a much larger frequency tuning range than
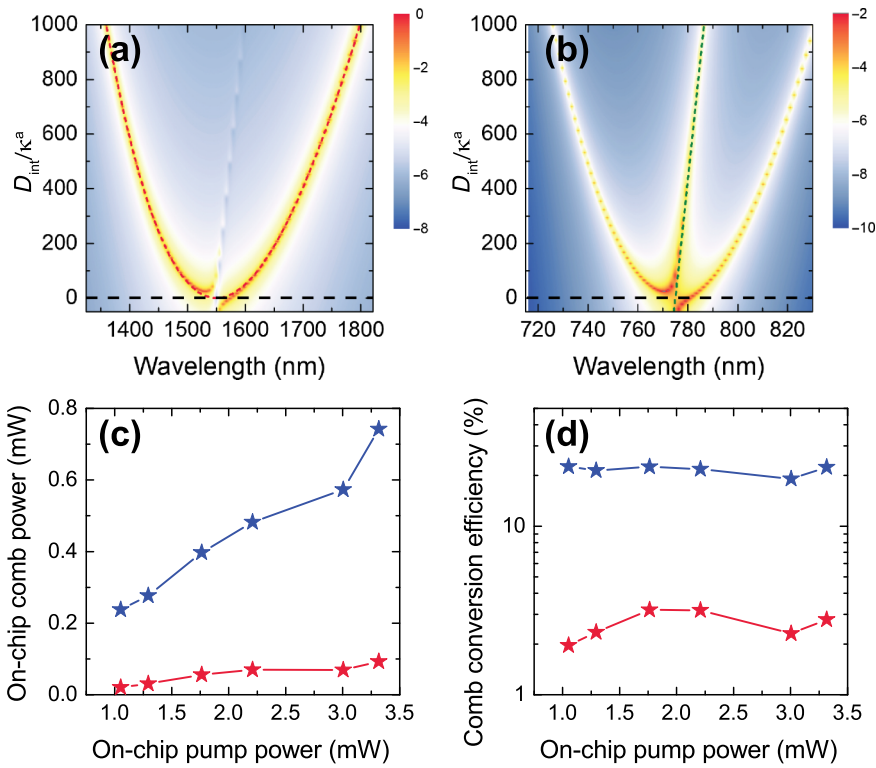
FIG. 4. Dual-band comb generation efficiency under different pump powers. (a) The density of states for the infrared modes (with a pump in the a_0 infrared mode) when the Cherenkov-like radiation is close to the second-harmonic wavelength of the pump. (b) The corresponding density of states for the near-visible mode. (c) Infrared (red) and near-visible (blue) comb powers under different pump powers. (d) On-chip conversion efficiency of the infrared (red) and near-visible (blue) combs. Here both the pump and the comb powers refer to the on-chip average powers. The on-chip peak power is around 1000 times higher than the average power considering a pulse duty cycle of 1/1000.

by mechanical actuation [52] or electro-optic effects [53]. Figures 5(a) and 5(c) show the infrared and near-visible comb spectra for different temperatures. The measured thermal shifting of the infrared comb lines is 2.62 GHz/K. Considering the free spectral range of 726.7 GHz, a temperature tuning range of 277.4 K is needed to shift the infrared comb by one free spectral range. The near-visible comb lines, however, have a thermal shifting (5.24 GHz/K) twice as large as the infrared comb line. This doubled thermal shifting can be explained by the three-wave mixing process where two of the infrared photons combine together to generate one near-visible photon. The enlarged insets of the spectra in Figs. 5(b) and 5(d) clearly show that the near-visible comb has been tuned by one free spectral range with thermal tuning while the infrared comb is tuned by half a free spectral range.

C. Visible comb spectroscopy

Spectroscopy is one of the important applications of an optical frequency comb. For biomedical sensing, which is predominantly in a water environment, visible optical combs are needed because of water's low absorption coefficient in this wavelength range. Here we show a proof-of-principle experiment of the frequency comb spectroscopy using our broadband, high-power near-visible comb. To validate this method, we firstly apply our near-visible comb to measure the transmission spectrum of a thin-film bandpass filter near 780 nm. By tuning the angle of the bandpass filter, the transmission band can be tuned continuously. After generating the near-visible comb on-chip, we send the comb through a fiber-to-fiber U-bench (Thorlabs FBC-780-APC) where the thin-film filter can be inserted. The experimental setup is shown in Supplemental Material Sec. IV. Here the near-visible comb spectrum through
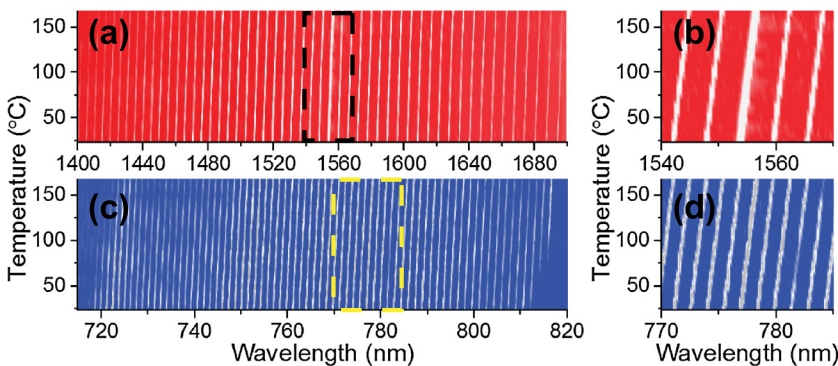

FIG. 5. Wavelength tuning of both infrared and near-visible frequency combs. (a),(b) The infrared frequency comb spectra for different temperatures of the device. Panel (b) shows an enlargement of the dashed box region in (a). (c),(d) The near-visible frequency comb spectra for different temperatures of the device. Panel (d) shows an enlargement of the dashed box region in (c).
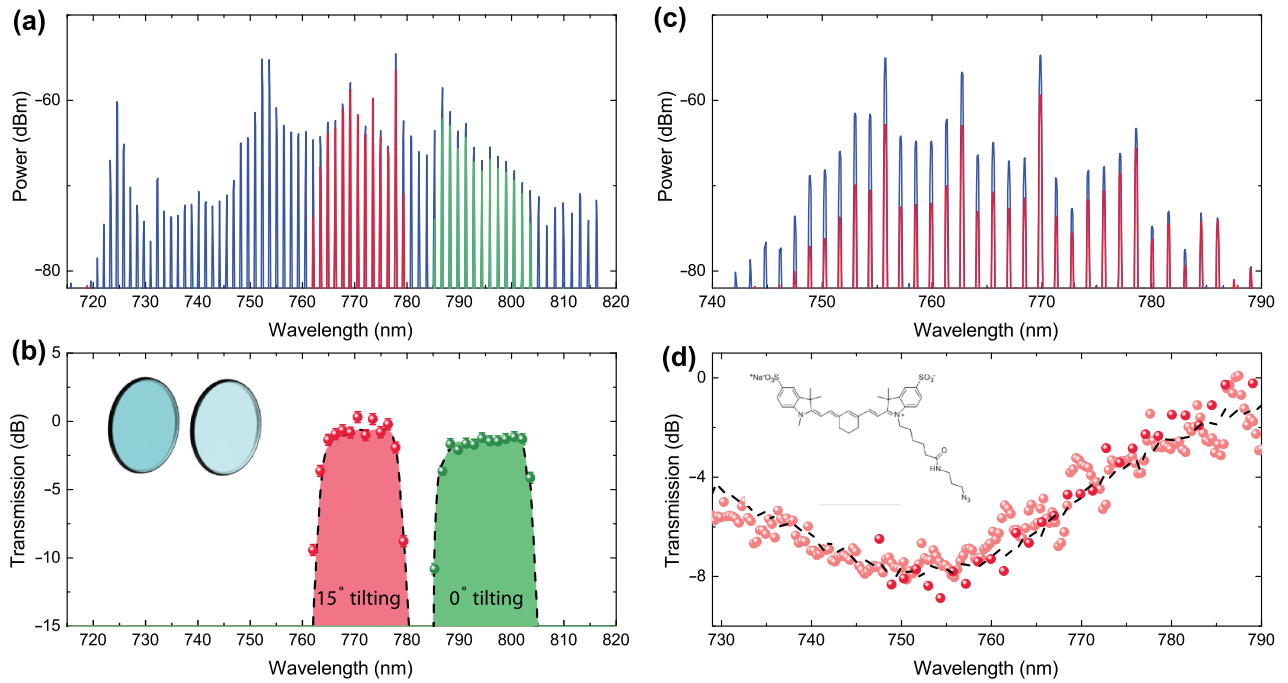
FIG. 6.   Comb spectroscopy in the near-visible range. (a) Near-visible comb spectra with and without the band pass filter. Blue line, original near-visible comb spectrum; green line, near-visible comb spectrum after 0° tilted thin-film bandpass filter; red line, near-visible comb spectrum after 15° tilted thin-film bandpass filter. (b) The measured transmission spectrum of the thin-film bandpass filter using comb spectroscopy (dots) and a Ti:sapphire laser (dashed lines). Inset: thin-film tunable filter. (c) Near-visible comb spectra passing through pure water (blue) or Cy-7 fluorescent dye solution (red). (d) The measured transmission spectrum of the Cy-7 fluorescent dye. Red dot, transmission spectrum extracted from the data shown in (c); pink dot, transmission spectrum extracted from the comb data measured by a high-sensitivity but low-resolution optical spectrum analyzer; dashed line, transmission spectrum measured by a tunable Ti:sapphire laser. Inset: the chemical formula of the used dye molecule.

an empty u-bench is measured as a reference, as shown by the blue line in Fig. 6(a). We then insert the thin-film filter inside the u-bench with either 0° or 15° tilting and measure the transmitted near-visible comb spectra afterward. As shown by the green and red lines in Fig. 6(a), the passband of the thin-film filter is tuned to shorter wavelengths with an increase of tilting angle. We can extract the transmission of the bandpass filter at the position of each comb line, as plotted in Fig. 6(b) with green and red circles. To independently calibrate the sample's absorption, we use a tunable Ti:sapphire laser (M2 Lasers SolsTiS) to measure the transmission spectrum of the bandpass filter, as shown by the dashed lines in Fig. 6(b). A good agreement between these two methods has been observed.

The near-visible microcomb is then used to measure the transmission spectrum of a water-solvable fluorescent dye molecule. The output of our near-visible comb is sent through a cuvette which contains either pure water or dye solution, and the transmitted comb spectra are measured as shown in Fig. 6(c). Comparing the comb's spectrum after passing through the dye solution [the red line in Fig. 6(c)] with the reference spectrum [the blue line in Fig. 6(c)], we can clearly see the wavelength-dependent absorption induced by the fluorescent dye molecule. We plot the comb

spectroscopy measurement result of this dye solution in Fig. 6(d), together with an independent measurement result using a Ti:sapphire laser [the dashed line in Fig. 6(d)]. A good agreement is obtained between the comb spectroscopy and the tunable Ti:sapphire laser, showing the validity of the visible comb spectroscopy in a water-based environment. Limited by the chaotic nature of the current combs, a more advanced spectroscopy experiment such as dual-comb spectroscopy [12,22] cannot yet be performed. Better device performance will be needed to allow us to generate the near-visible comb in the soliton regime, as will be discussed next.

IV. DISCUSSION AND CONCLUSION

The current device is operated in the chaotic regime, limited by the relatively high comb threshold power (300 mW). To operate in the mode-locked regime, further improvement of the quality factor is needed to lower the comb threshold. For example, our device has a relative narrow microring width, as required by the phase-matching condition. We anticipate that a smoother microring sidewall achieved by an improved fabrication recipe can largely help increase the quality factor of our device. Also,
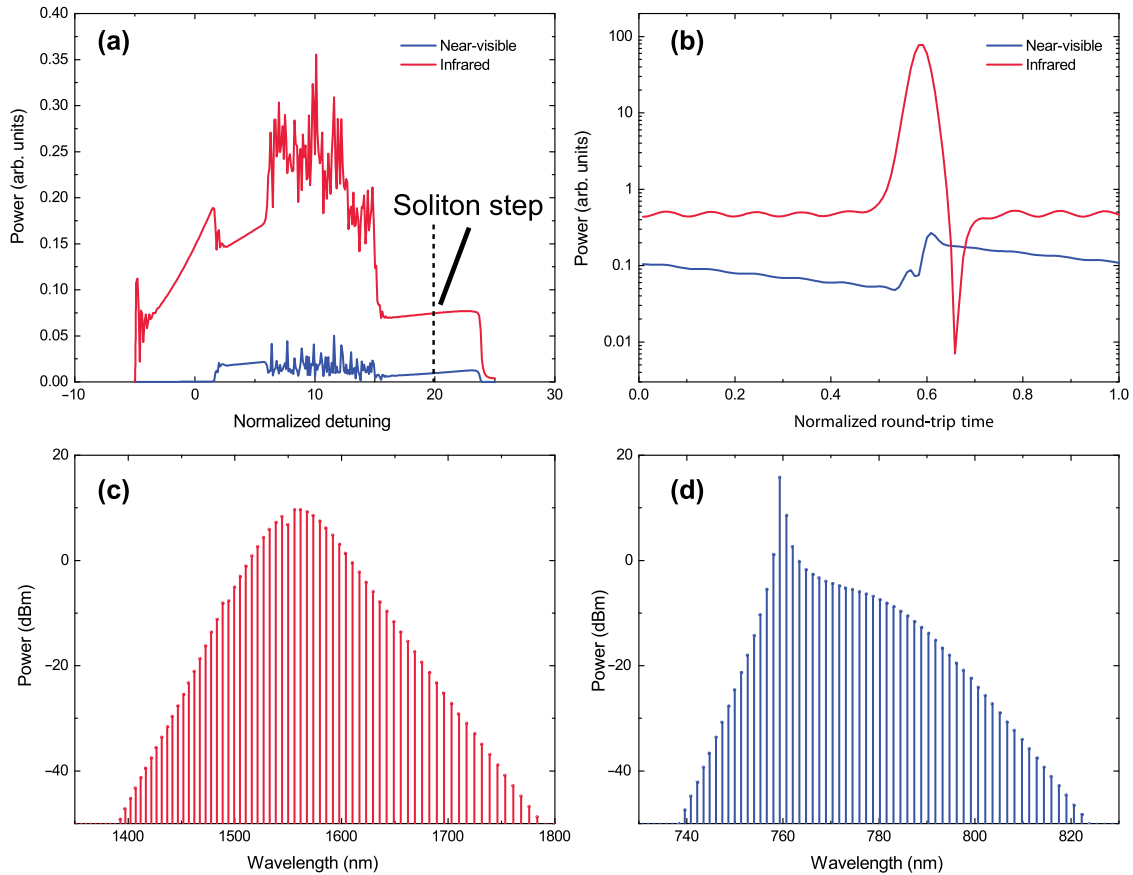
FIG. 7. Simulated dual-band comb spectrum under continuous-wave pumping. (a) The infrared (red) and near-visible (blue) comb powers in the cavity during the scan of the pump laser. (b) The time-domain pulse of a single soliton at both infrared (red) and near-visible (blue) wavelengths. (c) The spectrum of a single soliton in the infrared band. (d) The spectrum of the corresponding near-visible comb.

the thermal heating of the microring needs to be minimized to stably reach the soliton state [54]. Currently, our polycrystalline AlN devices possess much larger thermal heating than SiN devices [54], posing a challenge for operation of the device at coherent states. A single-crystal AlN platform [55], which possesses much smaller thermal heating as well as a higher quality factor, might be an ideal candidate for realizing coherent near-visible frequency comb generation.

We explore the soliton operation regime using numerical simulation assuming continuous-wave pumping. We scan the wavelength of the pump laser across the resonance and monitor the power in the cavity [Fig. 7(a)]. The pump power is set to be 2.5 W. We find a characteristic soliton step as noted in Fig. 7(a). We then show the system dynamics at a certain position in the soliton step. Figure 7(c) shows a clear infrared soliton spectrum and Fig. 7(d) shows the corresponding near-visible spectrum. The temporal pulse in the cavity (Fig. 7(b)) clearly shows the co-propagating infrared/near-visible soliton behavior in the microring resonator. This result shows that dual-band

soliton generation can, in principle, be realized in our system.

In conclusion, our experiment shows a scheme to generate a high-power microcomb in the near-visible wavelength range, which is beneficial for realizing f-$2f$ self-referencing on a single chip, for example by beating an octave spanning TM_0 mode Kerr comb and a TM_2 mode near-visible comb. The thermal tuning demonstrated can be an efficient way to control the carrier-envelope offset frequency. With an *in situ*, Cherenkov-like radiation enhanced frequency up-conversion process, the near-visible comb line power can be high enough, eliminating bulky equipment for external laser transfer and frequency conversion [23]. The ability to realize high-efficiency $\chi^{(2)}$ and $\chi^{(3)}$ nonlinear processes in a single microresonator opens the door for extending the Kerr frequency comb into both shorter and longer wavelength ranges and it is possible to realize multioctave optical frequency comb generation from a single on-chip device. When the thermal effect can be overcome, numerical simulation [56] suggests the potential to realize soli-

ton generation simultaneously at two wavelength bands. Future studies in this direction may include more coherent nonlinear effects in a single microresonator, such as third-harmonic generation, Raman scattering, and electro-optical effects.

ACKNOWLEDGMENTS

APPENDIX A: DEVICE DESIGN AND FABRICATION

For efficient frequency comb generation at near-visible wavelengths, the device geometry should be engineered to realize the anomalous dispersion for the fundamental (TM_0) modes at the pump wavelength, as well as the phase-matching condition between the fundamental modes at the infrared band and the high-order (TM_2) modes at the near-visible band. We design the microring width varying from 1.12 to 1.21 μm, for which parameters the anomalous dispersion is always achieved while the Cherenkov-like radiation wavelength is continuously tuned. For the convenience of fabricating and characterizing the microring with different geometry parameters, there are eight microring resonators in each bus waveguide set. To avoid the overlap of the resonances for different microring resonators in the same bus waveguide set, the radii of the cascaded microrings are offset by 9 nm, which results in an offset of resonance wavelength by 0.4 nm. As a result, the resonances of the eight microrings are well separated in the frequency domain and can be selectively pumped by tuning the pump laser wavelength. There are two waveguides coupled with the microring resonator. One wrap-around waveguide tapered from 0.175 to 0.125 μm or from 0.15 to 0.1 μm is used to efficiently extract the near-visible light from the resonator, with a coupling gap varying from 0.3 to 0.5 μm. The width of the other bus waveguide is fixed to be 0.8 μm with a gap of 0.6 μm, realizing critical coupling for the pump light in the infrared band. The base radius (with no offset) of the microrings is fixed to be 30 μm.

Our device is fabricated using AlN on SiO_2 on a silicon wafer. The nominal AlN film thickness is 1 μm, while the measured thickness is 1.055 μm. After defining the pattern with FOx 16 (Dow Corning, USA) using electron beam lithography, the waveguide and microring resonators are dry etched using $Cl_2/BCl_3/Ar$ chemistry, and then a 1-μm-thick PECVD oxide is deposited on top of the AlN waveguide. The chip is annealed in N_2 atmosphere for 2 h at 950 °C to improve the quality factors of the optical modes.

APPENDIX B: DETAILS OF MEASUREMENT PROCESS

The pump laser pulse is generated by amplifying a 10 ns square pulse (duty cycle 1/1000) in two stages of erbium-doped fiber amplifiers. Tunable bandpass filters are inserted after each amplification stage to remove the amplified spontaneous emission noise. Due to the low average power of the pulses, the peak power of the optical pulse can be amplified to more than 10 W. The seeding pulse is obtained by modulating the output of a continuous-wave infrared laser (New Focus TLB-6728) with an electro-optic modulator. The 10 ns pulse duration time is much longer than the cavity lifetime (1 ns) of our microring cavity, leading to a quasicontinuous wave pump for the optical modes. The optical comb spectra are measured by an optical spectra analyzer which has a measurement span of 600 to 1700 nm. To avoid cross talk in the optical spectrum analyzer, we used a long-pass (short-pass) filter to block all the near-visible (infrared) light when we measure the infrared (near-visible) comb spectrum. Our chip sits on top of a close-loop temperature control unit (Covesion OC2) which has a thermal stability of 0.01 ° C and a thermal tuning range from room temperature to 200 °C. The used thin-film bandpass filter is a VersaChrome filter (with a center wavelength of 790 nm and a bandwidth of 12 nm) from Semrock and the fluorescent dye is sulfo-Cyanine7 from Lumiprobe.

[1] T. Udem, R. Holzwarth, and T. W. Hänsch, Optical frequency metrology, Nature **416**, 233 (2002).

[2] A. Schliesser, N. Picqué, and T. W. Hänsch, Mid-infrared frequency combs, Nat. Photonics **6**, 440 (2012).

[3] V. Torres-Company and A. M. Weiner, Optical frequency comb technology for ultra-broadband radio-frequency photonics, Laser Photon. Rev. **8**, 368 (2014).

[4] J. Pfeifle, V. Brasch, M. Lauermann, Y. Yu, D. Wegner, T. Herr, K. Hartinger, P. Schindler, J. Li, D. Hillerkuss, R. Schmogrow, C. Weimann, R. Holzwarth, W. Freude, J. Leuthold, T. J. Kippenberg, and C. Koos, Coherent terabit communications with micro resonator Kerr frequency combs, Nat. Photonics **8**, 375 (2014).

[5] Z. Jiang, C.-B. Huang, D. E. Leaird, and A. M. Weiner, Optical arbitrary waveform processing of more than 100 spectral comb lines, Nat. Photonics **1**, 463 (2007).

[6] A. A. Savchenkov, A. B. Matsko, V. S. Ilchenko, I. Solomatine, D. Seidel, and L. Maleki, Tunable Optical Frequency Comb with a Crystalline Whispering Gallery Mode Resonator, Phys. Rev. Lett. **101**, 093902 (2008).

[7] W. Liang, D. Eliyahu, V. S. Ilchenko, A. A. Savchenkov, A. B. Matsko, D. Seidel, and L. Maleki, High spectral purity Kerr frequency comb radio frequency photonic oscillator, Nat. Commun. **6**, 7957 (2015).

[8] C.-h. Li, A. J. Benedick, P. Fendel, A. G. Glenday, F. X. Kärtner, D. F. Phillips, D. Sasselov, A. Szentgyorgyi, and R. L. Walsworth, A laser frequency comb that enables radial velocity measurements with a precision of 1 cm s^{-1}, Nature **452**, 610 (2008).

[9] A. Bartels, D. Heinecke, and S. a. Diddams, 10-GHz self-referenced optical frequency comb, Science **326**, 681 (2009).

[10] F. Keilmann, C. Gohle, and R. Holzwarth, Time-domain mid-infrared frequency-comb spectrometer, Opt. Lett. **29**, 1542 (2004).

[11] S. Potvin and J. Genest, Dual-comb spectroscopy using frequency-doubled combs around 775 nm, Opt. Express **21**, 30707 (2013).

[12] M.-G. Suh, Q.-F. Yang, K. Y. Yang, X. Yi, and K. J. Vahala, Microresonator soliton dual-comb spectroscopy, Science **354**, 600 (2016).

[13] P. Del'Haye, A. Schliesser, O. Arcizet, T. Wilken, R. Holzwarth, and T. J. Kippenberg, Optical frequency comb generation from a monolithic microresonator, Nature **450**, 1214 (2007).

[14] T. J. Kippenberg, R. Holzwarth, and S. A. Diddams, Microresonator-based optical frequency combs, Science **332**, 555 (2011).

[15] P. Del'Haye, T. Herr, E. Gavartin, M. L. Gorodetsky, R. Holzwarth, and T. J. Kippenberg, Octave Spanning Tunable Frequency Comb from a Microresonator, Phys. Rev. Lett. **107**, 063901 (2011).

[16] Y. Okawachi, K. Saha, J. S. Levy, Y. H. Wen, M. Lipson, and A. L. Gaeta, Octave-spanning frequency comb generation in a silicon nitride chip, Opt. Lett. **36**, 3398 (2011).

[17] T. Herr, V. Brasch, J. D. Jost, C. Y. Wang, N. M. Kondratiev, M. L. Gorodetsky, and T. J. Kippenberg, Temporal solitons in optical microresonators, Nat. Photonics **8**, 145 (2013).

[18] X. Xue, Y. Xuan, Y. Liu, P.-H. Wang, S. Chen, J. Wang, D. E. Leaird, M. Qi, and A. M. Weiner, Mode-locked dark pulse Kerr combs in normal-dispersion microresonators, Nat. Photonics **9**, 594 (2015).

[19] X. Yi, Q.-F. Yang, K. Y. Yang, M.-G. Suh, and K. Vahala, Soliton frequency comb at microwave rates in a high-Q silica microresonator, Optica **2**, 1078 (2015).

[20] V. Brasch, M. Geiselmann, T. Herr, G. Lihachev, M. H. P. Pfeiffer, M. L. Gorodetsky, and T. J. Kippenberg, Photonic chip-based optical frequency comb using soliton Cherenkov radiation, Science **351**, 357 (2016).

[21] Q.-F. Yang, X. Yi, K. Y. Yang, and K. Vahala, Stokes solitons in optical microcavities, Nat. Phys. **1**, 1 (2016).

[22] M. Yu, Y. Okawachi, A. G. Griffith, N. Picqué, M. Lipson, and A. L. Gaeta, Silicon-chip-based mid-infrared dual-comb spectroscopy, arXiv:1610.01121

[23] V. Brasch, E. Lucas, J. D. Jost, M. Geiselmann, and T. J. Kippenberg, Self-referenced photonic chip soliton Kerr frequency comb, Light Sci. Appl. **6**, e16202 (2016).

[24] A. Coillet, J. Dudley, G. Genty, L. Larger, and Y. K. Chembo, Optical rogue waves in whispering-gallery-mode resonators, Phys. Rev. A **89**, 013835 (2014).

[25] C. Godey, I. V. Balakireva, A. Coillet, and Y. K. Chembo, Stability analysis of the spatiotemporal Lugiato-Lefever model for Kerr optical frequency combs in the anomalous and normal dispersion regimes, Phys. Rev. A **89**, 063814 (2014).

[26] C. Bao, J. A. Jaramillo-Villegas, Y. Xuan, D. E. Leaird, M. Qi, and A. M. Weiner, Observation of Fermi-Pasta-Ulam Recurrence Induced by Breather Solitons in an Optical Microresonator, Phys. Rev. Lett. **117**, 163901 (2016).

[27] M. Yu, J. K. Jang, Y. Okawachi, A. G. Griffith, K. Luke, S. A. Miller, X. Ji, M. Lipson, and A. L. Gaeta, Breather soliton dynamics in microresonators, arxiv:1609.01760.

[28] E. Lucas, M. Karpov, H. Guo, M. Gorodetsky, and T. Kippenberg, Breathing dissipative solitons in optical microresonators, arXiv:1611.06567.

[29] A. F. Fercher, W. Drexler, C. K. Hitzenberger, and T. Lasser, Optical coherence tomography-principles and applications, Rep. Prog. Phys. **66**, 239 (2003).

[30] J. Vanier, Atomic clocks based on coherent population trapping: A review, Appl. Phys. B **81**, 421 (2005).

[31] A. A. Savchenkov, A. B. Matsko, W. Liang, V. S. Ilchenko, D. Seidel, and L. Maleki, Kerr combs with selectable central frequency, Nat. Photonics **5**, 293 (2011).

[32] Y. Yang, X. Jiang, S. Kasumie, G. Zhao, L. Xu, J. M. Ward, L. Yang, and S. N. Chormaic, Four-wave mixing parametric oscillation and frequency comb generation at visible wavelengths in a silica microbubble resonator, Opt. Lett. **41**, 5266 (2016).

[33] X. Guo, C.-L. Zou, and H. X. Tang, Second-harmonic generation in aluminum nitride microrings with 2500%/W conversion efficiency, Optica **3**, 1126 (2016).

[34] X. Guo, C.-L. Zou, H. Jung, and H. X. Tang, On-Chip Strong Coupling and Efficient Frequency Conversion between Telecom and Visible Optical Modes, Phys. Rev. Lett. **117**, 123902 (2016).

[35] X. Guo, C.-l. Zou, C. Schuck, H. Jung, R. Cheng, and H. X. Tang, Parametric down-conversion photon-pair source on a nanophotonic chip, Light Sci. Appl. **6**, e16249 (2017).

[36] H. Jung, X. Guo, N. Zhu, S. B. Papp, S. A. Diddams, and H. X. Tang, Phase-dependent interference between frequency doubled comb lines in a $\chi^{(2)}$ phase-matched aluminum nitride microring, Opt. Lett. **41**, 3747 (2016).

[37] H. Jung, R. Stoll, X. Guo, D. Fischer, and H. X. Tang, Green, red, and IR frequency comb line generation from single IR pump in AlN microring resonator, Optica **1**, 396 (2014).

[38] S. Miller, K. Luke, Y. Okawachi, J. Cardenas, A. L. Gaeta, and M. Lipson, On-chip frequency comb generation at visible wavelengths via simultaneous second- and third-order optical nonlinearities, Opt. Express **22**, 26517 (2014).

[39] X. Xue, F. Leo, Y. Xuan, J. A. Jaramillo-Villegas, P.-H. Wang, D. E. Leaird, M. Erkintalo, M. Qi, and A. M. Weiner, Second-harmonic assisted four-wave mixing in chip-based microresonator frequency comb generation, Light Sci. Appl. **6**, e16253 (2017).

[40] L. Wang, L. Chang, N. Volet, M. H. P. Pfeiffer, M. Zervas, H. Guo, T. J. Kippenberg, and J. E. Bowers, Frequency comb generation in the green using silicon nitride microresonators, Laser Photon. Rev. **10**, 631 (2016).

[41] P. Del'Haye, A. Coillet, T. Fortier, K. Beha, D. C. Cole, K. Y. Yang, H. Lee, K. J. Vahala, S. B. Papp, and S. A. Diddams, Phase-coherent microwave-to-optical link with a self-referenced microcomb, Nat. Photonics **10**, 516 (2016).

[42] M. Pu, L. Ottaviano, E. Semenova, and K. Yvind, Efficient frequency comb generation in AlGaAs-on-insulator, Optica **3**, 823 (2016).

[43] Y. K. Chembo, D. V. Strekalov, and N. Yu, Spectrum and Dynamics of Optical Frequency Combs Generated with Monolithic Whispering Gallery Mode Resonators, Phys. Rev. Lett. **104**, 103902 (2010).

[44] Y. K. Chembo and N. Yu, Modal expansion approach to optical-frequency-comb generation with monolithic whispering-gallery-mode resonators, Phys. Rev. A **82**, 33801 (2010).

[45] H. Guo, M. Karpov, E. Lucas, A. Kordts, M. H. P. Pfeiffer, V. Brasch, G. Lihachev, V. E. Lobanov, M. L. Gorodetsky, and T. J. Kippenberg, Universal dynamics and deterministic switching of dissipative Kerr solitons in optical microresonators, Nat. Phys. **1**, 1 (2016).

[46] See Supplemental Material at http://link.aps.org/supplemental/10.1103/PhysRevApplied.10.014012 for theoretical derivation, numerical simulation, experimental setup, and additional measurement data.

[47] A. B. Matsko, W. Liang, A. A. Savchenkov, D. Eliyahu, and L. Maleki, Optical Cherenkov radiation in overmoded microresonators, Opt. Lett. **41**, 2907 (2016).

[48] M. Erkintalo, Y. Q. Xu, S. G. Murdoch, J. M. Dudley, and G. Genty, Cascaded Phase Matching and Nonlinear Symmetry Breaking in Fiber Frequency Combs, Phys. Rev. Lett. **109**, 223904 (2012).

[49] S. Coen, H. G. Randle, T. Sylvestre, and M. Erkintalo, Modeling of octave-spanning Kerr frequency combs using a generalized mean-field Lugiato-Lefever model, Opt. Lett. **38**, 37 (2013).

[50] Q.-F. Yang, X. Yi, K. Y. Yang, and K. Vahala, Spatial-mode-interaction-induced dispersive waves and their active tuning in microresonators, Optica **3**, 1132 (2016).

[51] X. Xue, Y. Xuan, C. Wang, P.-H. Wang, Y. Liu, B. Niu, D. E. Leaird, M. Qi, and A. M. Weiner, Thermal tuning of Kerr frequency combs in silicon nitride microring resonators, Opt. Express **24**, 687 (2016).

[52] S. B. Papp, P. Del'Haye, and S. A. Diddams, Mechanical Control of a Microrod-Resonator Optical Frequency Comb, Physical Review X **3**, 031003 (2013).

[53] H. Jung, K. Y. Fong, C. Xiong, and H. X. Tang, Electrical tuning and switching of an optical frequency comb generated in aluminum nitride microring resonators, Opt. Lett. **39**, 84 (2014).

[54] Q. Li, T. C. Briles, D. A. Westly, T. E. Drake, J. R. Stone, B. R. Ilic, S. A. Diddams, S. B. Papp, and K. Srinivasan, Stably accessing octave-spanning microresonator frequency combs in the soliton regime, Optica **4**, 193 (2017).

[55] X. Liu, C. Sun, B. Xiong, L. Wang, J. Wang, Y. Han, Z. Hao, H. Li, Y. Luo, J. Yan, T. Wei, Y. Zhang, and J. Wang, Integrated continuous-wave aluminum nitride Raman laser, Optica **4**, 893 (2017).

[56] C.-l. Zou, X. Guo, L. Jiang, and H. X. Tang, The simulation of microcomb generation by multiple mode families, In preparation (2017).